Metal-Organic Framework/Graphene Oxide composites for CO_2 Capture by Microwave Swing Adsorption

Supporting information

Mégane Muschi[a], Sabine Devautour-Vinot[b], Damien Aureau[c], Nicolas Heymans[d], Saad Sene[a], Rudolf Emmerich[e], Alexandros Ploumistos[a], Amine Geneste[b], Nathalie Steunou[a,c], Gilles Patriarche[f], Guy De Weireld[d], Christian Serre*[a]

a. Institut des Matériaux Poreux de Paris, ESPCI Paris, Ecole Normale Supérieure, CNRS, PSL University, 75005 Paris, France.
b. ICGM, Univ. Montpellier, CNRS, ENSCM, Montpellier, France.
c. Institut Lavoisier de Versailles, UMR 8180 CNRS, Université de Versailles St Quentin en Yvelines, Université Paris Saclay, Versailles, France.
d. Service de Thermodynamique et de Physique mathématique, Faculté Polytechnique, Université de Mons, 7000 Mons, Belgium.
e. Fraunhofer Institute for Chemical Technology ICT Joseph-von-Fraunhofer St. 7, 76327 Pfinztal, Germany.
f. Université Paris-Saclay, CNRS, Centre de Nanosciences et de Nanotechnologies, 91120, Palaiseau, France.

* Corresponding author: christian.serre@espci.psl.eu

Table of contents

Characterizations

PXRD data for general characterization were recorded on PANalytical EMPYREAN diffractometer with CuKα radiation (λ = 1.5418 Å) and equipped with a PIXcel 1D detector. Nitrogen porosimetry data were collected on a Micromeritics Tristar instrument at 77 K. (Micromeritics Instrument Corporation) equipped with a Smart VacPrep outgassing unit. Pure carbon dioxide and nitrogen sorption measurements were conducted at 303 K with a 3Flex volumetric adsorption analyzer (Micromeritics Instrument Corporation) equipped with a Smart VacPrep outgassing unit. Thermogravimetric data were collected on Mettler Toledo TGA/DSC 2, STAR System apparatus with a heating rate of 3 °C/min under nitrogen flow. TEM/STEM observations were made on a Titan Themis 200 microscope (FEI/ Thermo Fischer Scientific) equipped with a geometric aberration corrector on the probe. The microscope is also equipped with the "Super-X" systems for EDX analysis with a detection angle of 0.9 steradian. The observations are made at 200 kV with a probe current of about 70 pA and a half-angle of convergence of 24 mrad. HAADF-STEM images are acquired with a camera length of 110 mm (inner/outer collection angles are respectively 69 and 200 mrad). The TEM images and the Electron Diffraction patterns are recorded with a Ceta 16M camera from Thermo Fisher (4k x 4k CMOS sensor). The samples were deposited on pure carbon membrane. X-ray Photoelectron Spectroscopy measurements were carried out using a Thermofisher Scientific ESCALab 250 Xi spectrometer with a monochromatic Al-Kα X-ray source (hν = 1486.6 eV) using a 650 µm spot (ILV, Versailles). The detection was performed perpendicularly to the sample surface using a constant analyzer energy (CAE) mode (pass energy 100 eV for survey and 20 eV for high resolution). Spectra were recorded with a 0.1 eV energy step. The use of low-energy electron and ion flood gun was necessary to perform the analysis.

Electrical measurements were performed on a Broadband Dielectric Spectrometer, Novocontrol alpha analyzer, using an applied *ac* voltage of 20 mV, over a frequency range from F = 10^{-1} Hz to F = 1 MHz, in the [273 K - 373 K] temperature domain. The data were collected using powders, which were introduced in a home-made sample holder, i.e. between two gold-coated electrodes in parallel plate capacitor configuration with an annular Teflon spacer for insulation. Prior to experiments, the materials were *in situ* treated at 373 K for 2 hours under dried nitrogen flux, in order to ensure that the residual solvent molecules were fully removed. The conductivity was determined considering the value collected at the *dc* plateau in the Bode representation of the real part of the conductivity. Typically, the real part of the *ac* conductivity results from the combination of three contributions: $\sigma_{ac}(\omega,T) = \sigma_{MWS}(\omega,T) + \sigma_{dc}(T) + \sigma'(\omega,T)$. The polarization component $\sigma'(\omega,T)$, corresponding to the increasing part of the signal at high frequency, arises from the local rearrangement of charges or dipoles causing dipolar reorientation. The *dc* conductivity plateau

$\sigma_{dc}(T)$, resulting from the long-range redistribution of charges dominates the intermediate frequency region. In case of highly ionic conductive materials, the Maxwell Wagner Sillars contribution $\sigma_{MWS}(\omega,T)$ due to the ionic charge accumulation to the sample/electrode interface is observed at low frequency. In insulators, $\sigma_{MWS}(\omega,T) \approx 0$ and $\sigma_{dc}(T) \approx 0$ and only the polarization conductivity is detectable, whereas in pure electronic conducting solids the *dc* plateau dominates the signal.

Desorption breakthrough measurements.

A homemade device was used to perform desorption curves (Figure S1). It is mainly composed of a borosilicate glass adsorption column (5 cm height (adjustable) and 1 cm diameter (Volume: 3.9 cm^3) – Omnifit Labware) containing the adsorbent, a gas supply system with three mass flow controllers [MFC] (one for helium, one for nitrogen and one for N_2/CO_2 mixture – Brooks Instrument: 0 – 10 Nl/h), a pressure sensor (PS), a Pt100 temperature sensor, a vacuum pump (VP) and a mass spectrometer [MS] (InProcess Instruments – GAM 200 with a mass range from 1 to 200 amu) to analyze gas composition at the outlet of the column. The mass spectrometer is calibrated before each set of measurements.

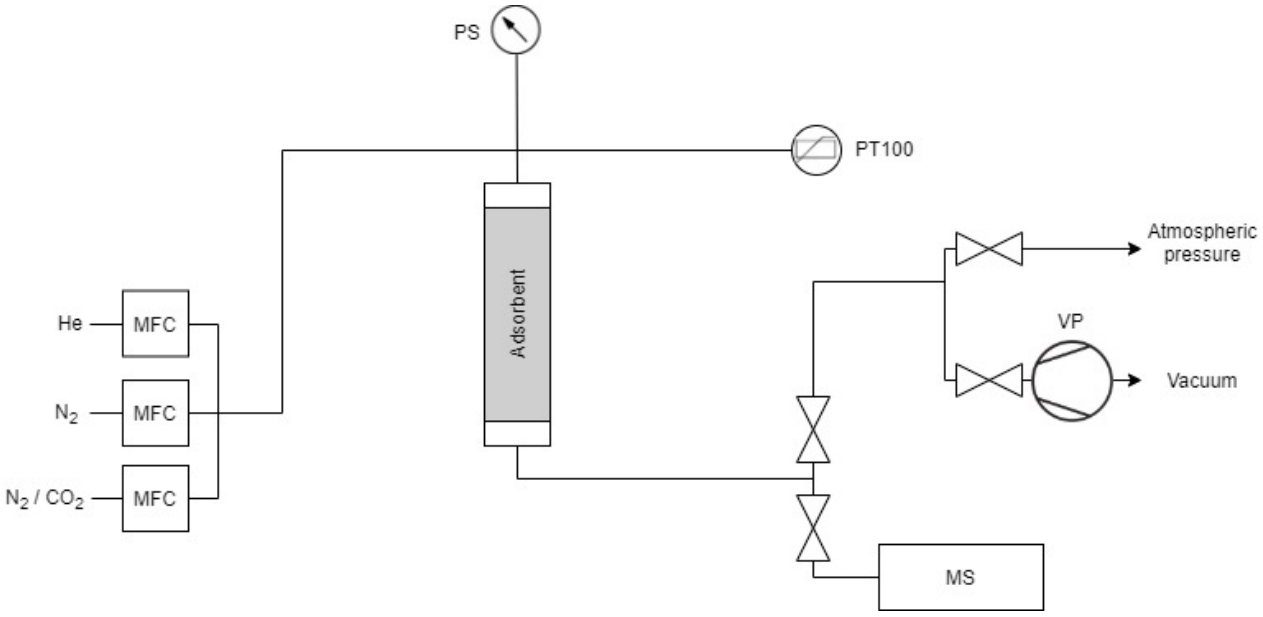

Figure S1. Experimental device for adsorption/desorption breakthrough curves measurements.

Prior to each measurement, the adsorbent is outgassed at set point temperature value (90°C for MIL-91(Ti)/GO and 50°C for UiO-66-btc(Zr)/GO) in an oven for 8 hours under primary vacuum. After cooling at room temperature, the adsorbent is saturated with a 2Nl/h N_2/CO_2 (85/15) flow (synthetic gas composition close to post-combustion ones).

Regarding desorption, two techniques were used to increase the temperature: conventional heating and microwave radiations. In each case, a 2Nl/h nitrogen flow is sent through the column. Regarding the conventional heating, the adsorption column is placed inside an oven and heated by setting a set point temperature value (50°C and 80 °C for MIL-91(Ti)/GO and 50 °C for UiO-66-btc(Zr)/GO) Regarding the microwave heating, the adsorption column is placed inside a single mode (dominant mode T10-Mode) microwave cavity connected with a magnetron with 2 kW power and equipped with an adjustable short to tune the cavity of maximum efficiency. The frequency was set at 2.45 GHz for all the experiments. A closed loop control is developed to heat the MOF/GO composite to a given temperature measured by an IR-sensor placed in a cavity hole. The microwave desorption conditions for each material are provided in table S1.

Table S1. Microwave desorption conditions to reach 50 °C.

Materials	Conditions
MIL-91(Ti)/GO5wt%	Continuous P = 250W to reach T, hold
UiO-66-btc(Zr)/GO10wt%	Pulsed P=390 W, t-Peak 200ms, t-Pause 1.2s

Cavity perturbation method

A home-made device was used to measure permittivity of the MOFs at 2.45 GHz as a function of temperature (20°C to 120°C). The device uses a rectangular waveguide cavity with TE10- mode as dominant field distribution (Figure S2). The quality factor Q_c, the resonant frequency f_c, the volume of the empty cavity (V_c) and of the sample volume (V_s) are well known. The material to be measured is introduced into the cavity at the position of maximum electric field and causes a reduction of the quality factor (Q_s) and the resonance frequency (f_s) (Figure S3). Because the contribution of the magnetic field can be ignored, the permittivity can be calculated with the formulas derived from perturbation theory (Figure S3). To measure the temperature dependency, the samples are heated outside the cavity in an oven to the given temperature and then introduced into the cavity.

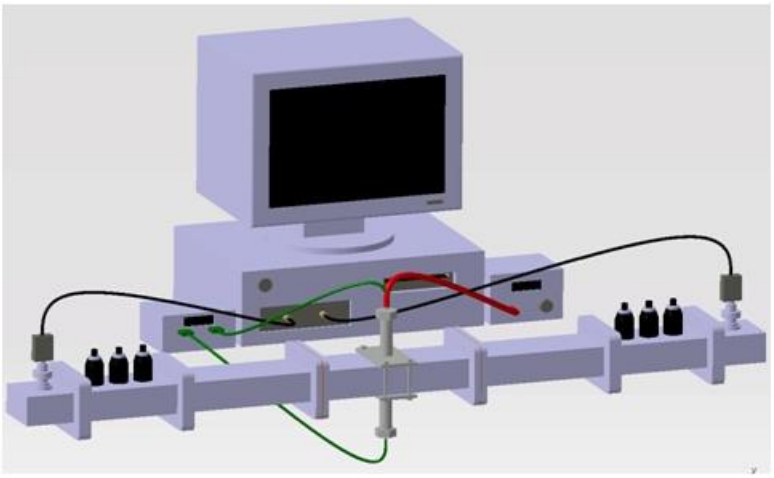

Figure S2. Device for measurement of the permittivity

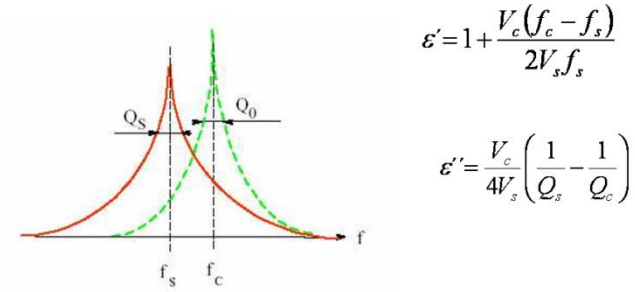

Figure S3. Schematic drawing of the measurement signals and formula for calculation

Results

MIL-91(Ti)/GO

The zeta-potential of MIL-91(Ti) depends on the pH with a positive surface charge below the point of zero charge (close to pH = 4) and negative surface charge above this value. This is due to the free P-OH groups of the MOF that get protonated at pH < 4 and deprotonated at pH > 4. On the other hand, the surface charge of GO is negative over almost the entire studied pH range, from very acidic pH, close to 1.5.

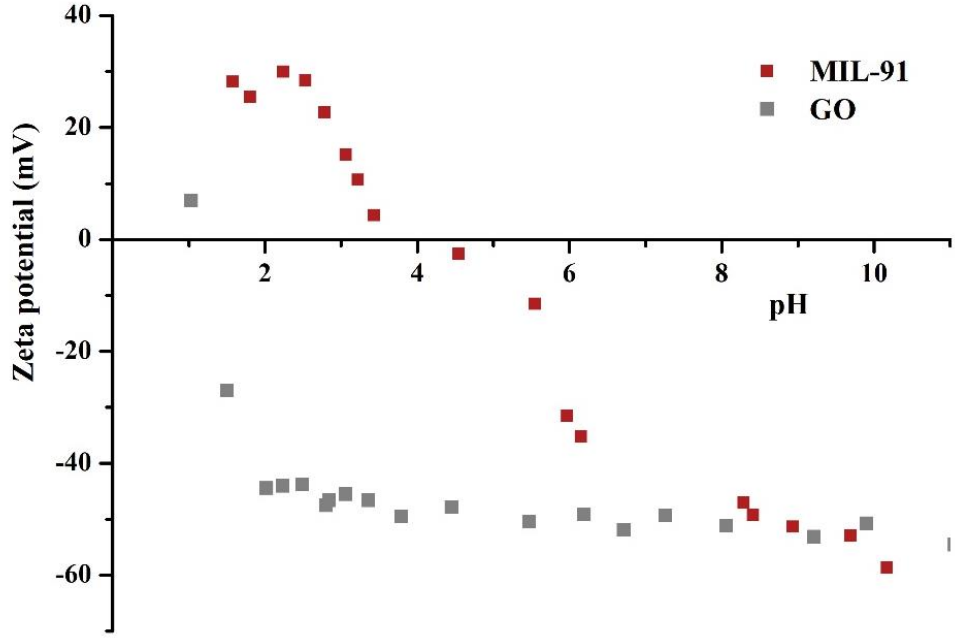

Figure S4. Zeta-potential as a function of pH of pure GO and pure MIL-91(Ti).

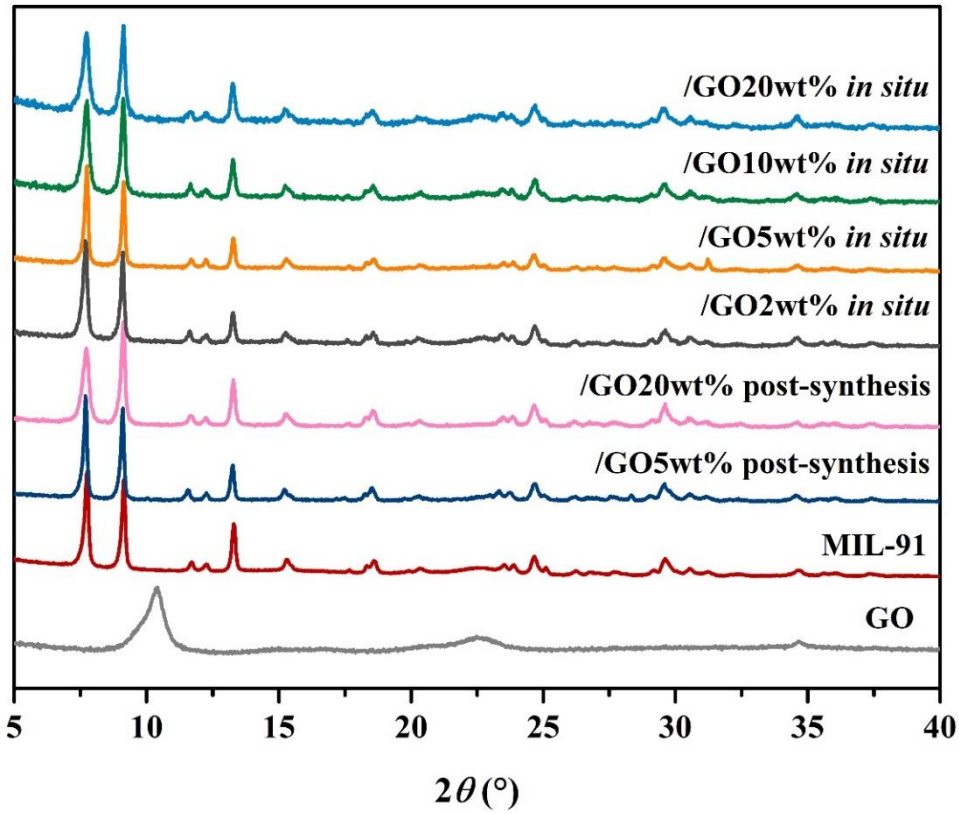

Figure S5. PXRD patterns (λ=1.5406 Å) of pure GO, pure MIL-91(Ti) and MIL-91(Ti)/GO composites. The broad peaks at 22.5°and 34.5° are due to the sample holder.

To confirm that the Bragg peaks width increases with the content of GO, the full width at half maximum (FWHM) of the peaks was measured for the *in situ* composites with 5 and 20wt% GO (Table S2). A slight increase is observed, in agreement with a decrease in particles size observed by TEM (Figure S6).

Table S2. Summary of the FWHM of the peaks between 0 ° and 16 ° for the MIL-91(Ti)/GO5 and 20wt% *in situ*.

		MIL-91/GO5wt% *in situ*	MIL-91/GO20wt% *in situ*
FWHM (°)	Peak at 7.7°	0.169	0.287
	Peak at 9.1°	0.113	0.170
	Peak at 11.7	0.221	0.224
	Peak at 12.3	0.171	0.244
	Peat at 13.3°	0.117	0.228
	Peat at 15.3°	0.291	0.431

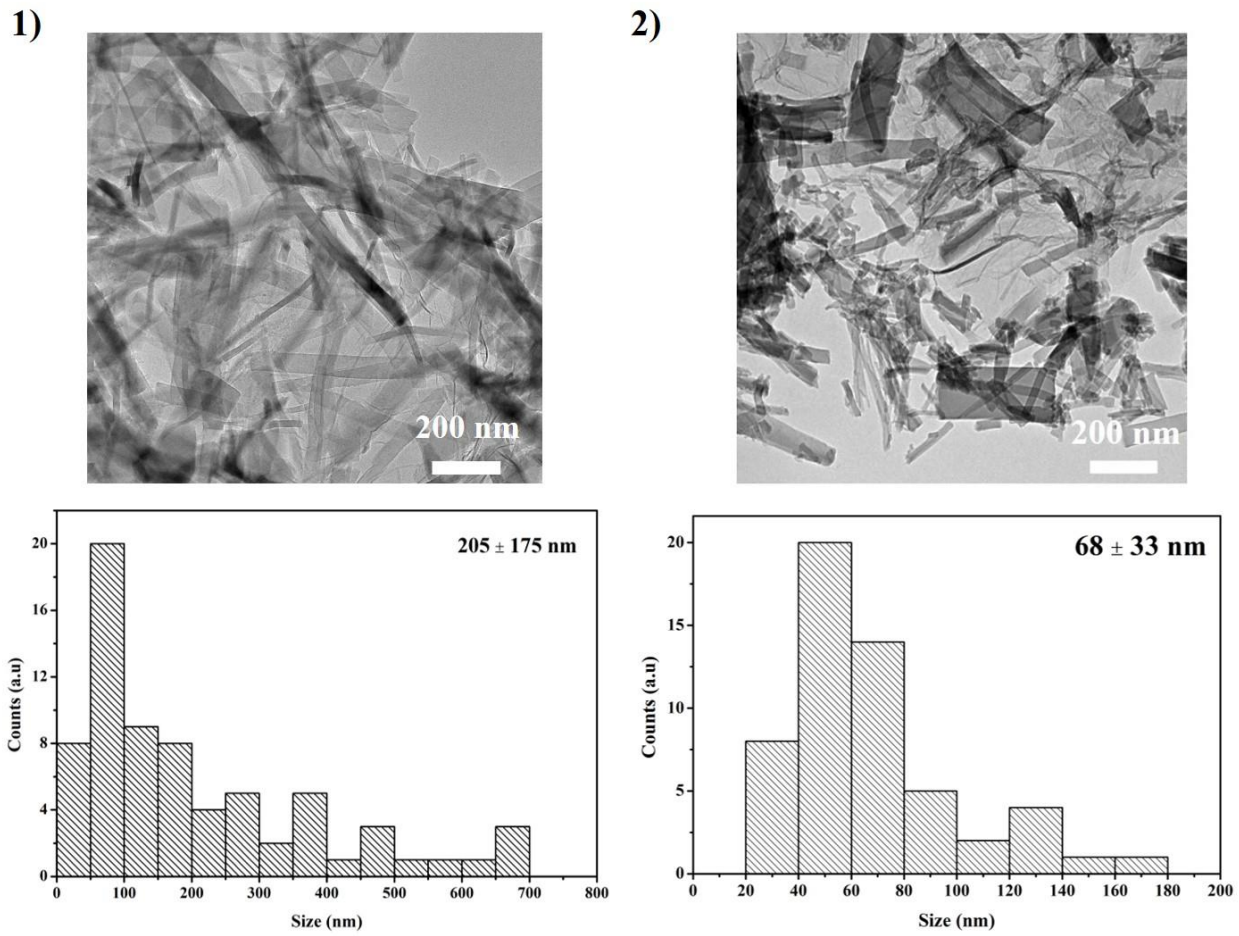

Figure S6. TEM images and diameter size distribution of 1) MIL-91(Ti)/GO5wt% *in situ* and 2) MIL-91(Ti)/GO20wt% *in situ*

The decrease in size of the MOF crystals when GO content increases has already been observed for other MOF/GO systems. [1,2] It was attributed to the coordination of the MOF metal to the COOH and OH groups of GO. As these groups provide nucleation sites for the MOF, it can be suggested that these nucleation sites are quite (i) close to each other and (ii) mostly located on GO, decreasing the content of MOF precursor in suspension which limit the Ostwald ripening of the MOF.

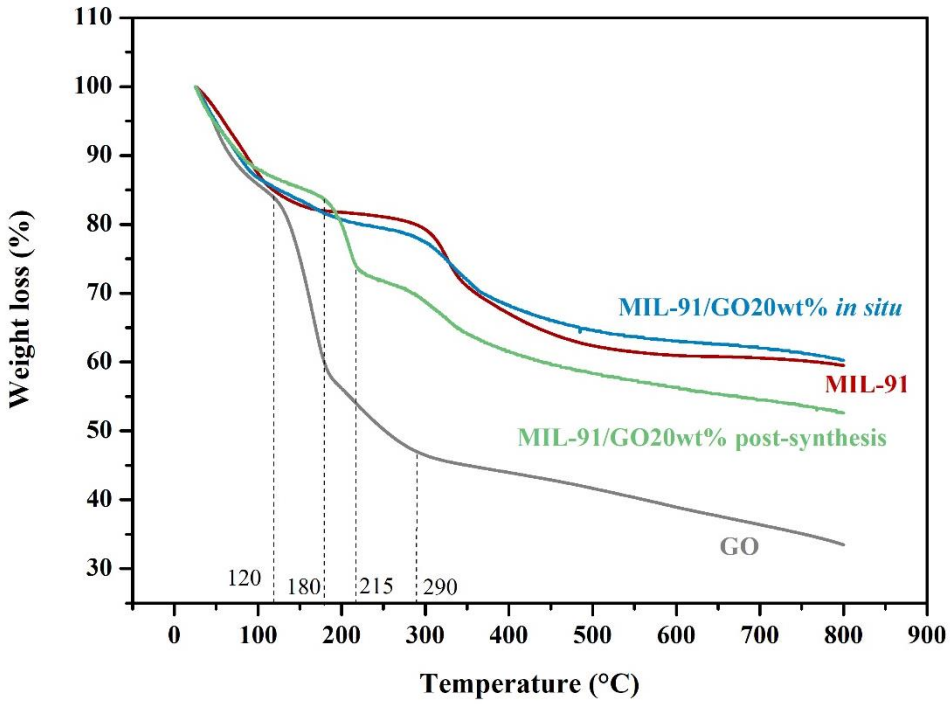

Figure S7. TGA curves under N_2 at 3 °C/min of pure GO, pure MIL-91(Ti) and MIL-91(Ti)/GO20wt% *in situ* and post-synthesis.

The TGA profiles of the composites were analyzed under nitrogen atmosphere. As shown in Figure S7, the bare MOF itself degrades at temperature above 250 °C. The TGA of pure GO shows several steps, in relation with the thermal stability of the different oxygenated groups. Below 120 °C, water is removed. Then, the most labile groups of GO are decomposed. From 180 °C, a second decomposition step can be observed. Finally, the less labile groups are removed from approximately 290 °C.

Note that at low GO loadings (< 10wt%) there are little to no differences between the composites due to the very low mass content of GO. However, at higher GO loading, such as 20wt%, the TGA profiles of the two composites exhibit differences (Figure S7). In both cases, the loss of oxygenated groups of GO tend to occur at higher temperatures in comparison with pure GO. This is due to interactions with the MOF particles that slightly stabilize the oxygen species. This phenomenon is more noticeable for *in situ* composite which suggests that the interactions between the MOF and the oxygen-bearing groups of GO nanosheets are stronger. Indeed, the post-synthesis composite shows one decomposition step that starts at 180 °C, which was attributed to the removal of the most labile groups of GO. A shift of 60 °C to higher temperatures compared to pure GO is thus observed, in agreement with the presence of electrostatic interactions between the two materials. The second step, at 215 °C, was attributed to the removal of the oxygen-bearing groups of GO which decomposed at 180 °C in pure GO. Then, decomposition of the MOF linker occurs around 280 °C,

similarly to the pure MOF. Regarding the *in situ* composite, no clear decomposition steps can be observed between 120 °C and 280 °C, temperature of which the MOF linker starts to degrade. It suggests that the departure of the most labile oxygen-bearing groups of GO occurs in the same temperature range as the MOF linker. This was attributed to the presence of direct coordination bonds between some oxygenated groups, such as carboxylic acids, and the titanium atoms from the MOF, as already observed for other metal cations/GO[3] and MOF/GO[4] systems.

Nitrogen porosimetry at 77 K

In addition to a decrease of BET surface areas when increasing the GO content, the adsorption isotherms show different shapes. While the MIL-91(Ti)/GO2wt% and MIL-91(Ti)/GO5wt% *in situ* composites show a type I isotherm in agreement with the microporosity of MIL-91(Ti), the two composites with 10 and 20wt% GO show a more distinct constant increase between $p/p_0 = 0.1$ and $p/p_0 = 0.8$. This can be attributed to the external surface area of GO and mesoporosity between the MOF particles and the GO sheets and/or between the GO sheets, as confirmed by the t-plot values (Table S3).

Table S3. BET surface area, micropore area, external surface area, micropore volume of MIL-91(Ti)/GO2, 5, 10 and 20wt%.

	MIL-91(Ti)/GO2wt% *in situ*	MIL-91(Ti)/GO5wt% *in situ*	MIL-91(Ti)/GO10wt% *in situ*	MIL-91(Ti)/GO20wt% *in situ*
BET surface area (m^2/g)	422	405	228	210
Micropore area (m^2/g)	404	380	186	144
External surface area (m^2/g)	18	25	42	66
Micropore volume (cm^3/g)	0.15	0.14	0.07	0.06

Electron microscopy and XPS

The MOF exhibits the same morphology within the two composites. However, they show different average sizes and, in both cases, a high polydispersity (Figure S6.1 and S10). Regarding the post-synthesis material, this polydispersity is intrinsic to the nucleation and growth mechanism of pure MIL-91(Ti). For the *in situ* sample, the presence of the GO sheets affects the nucleation and growth of the MOF crystals and leads to a larger average diameter size of the MOF compared to the pure MOF (Figure S6.1). However, there are several differences in the synthesis parameters (order of introduction of reactants, concentration) which can also impact the crystal size and polydispersity.

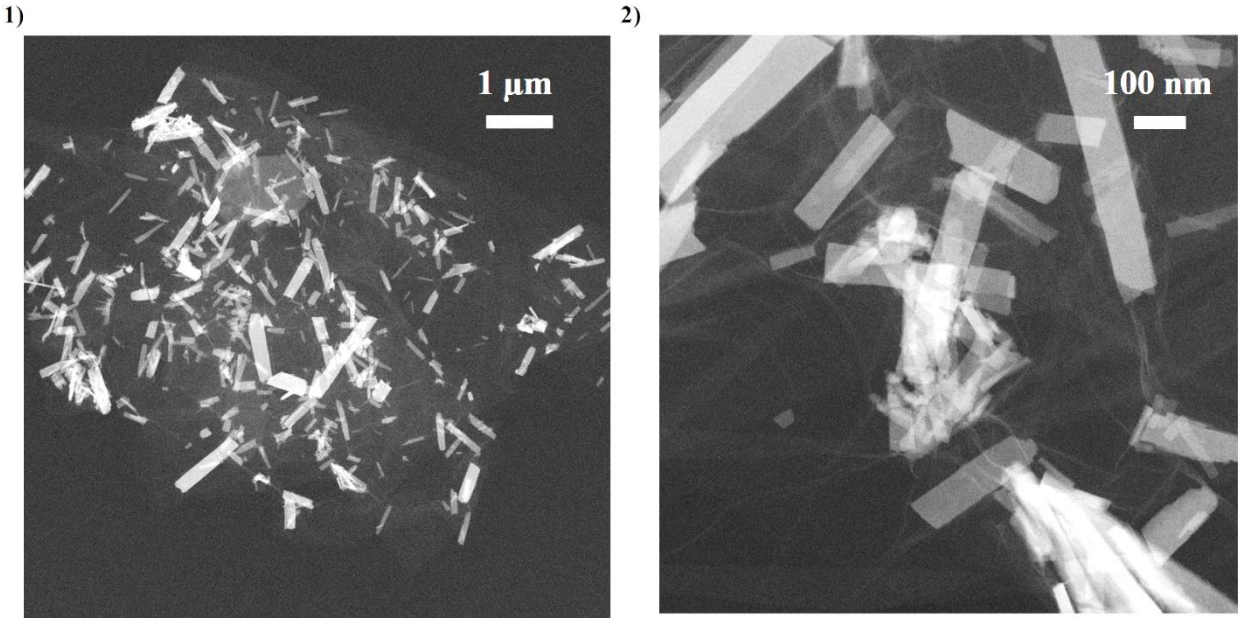

Figure S8. 1) and 2) STEM-HAADF images of MIL-91(Ti)/GO5wt% post-synthesis.

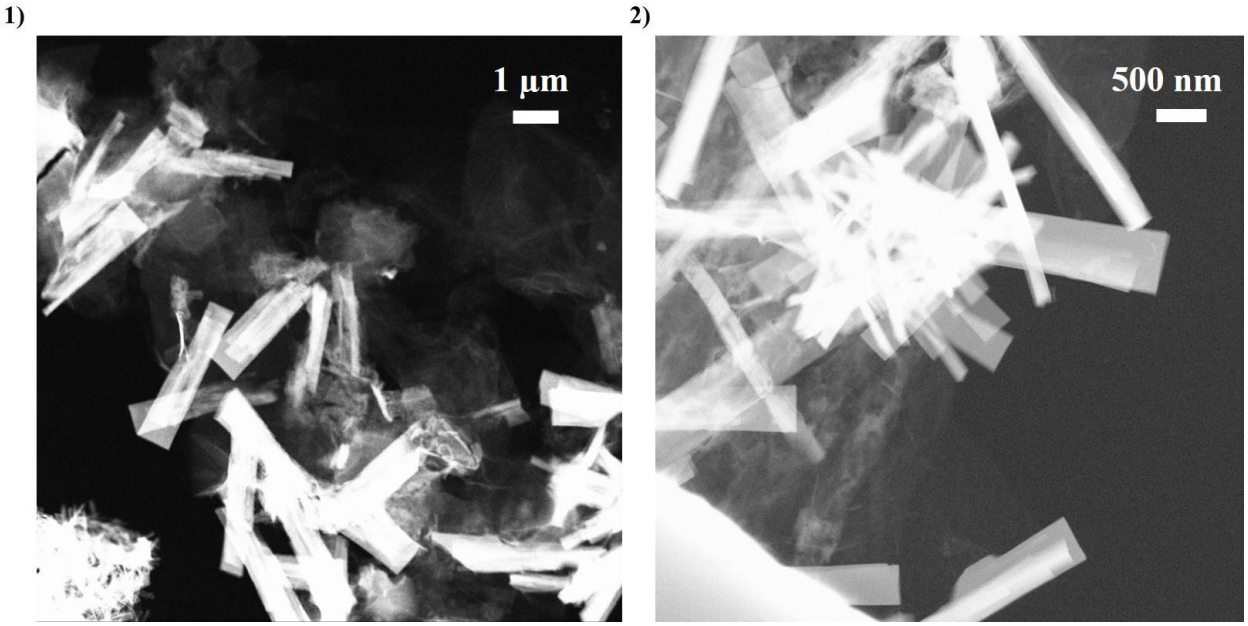

Figure S9. 1) and 2) STEM-HAADF images of MIL-91(Ti)/GO5wt% *in situ*.

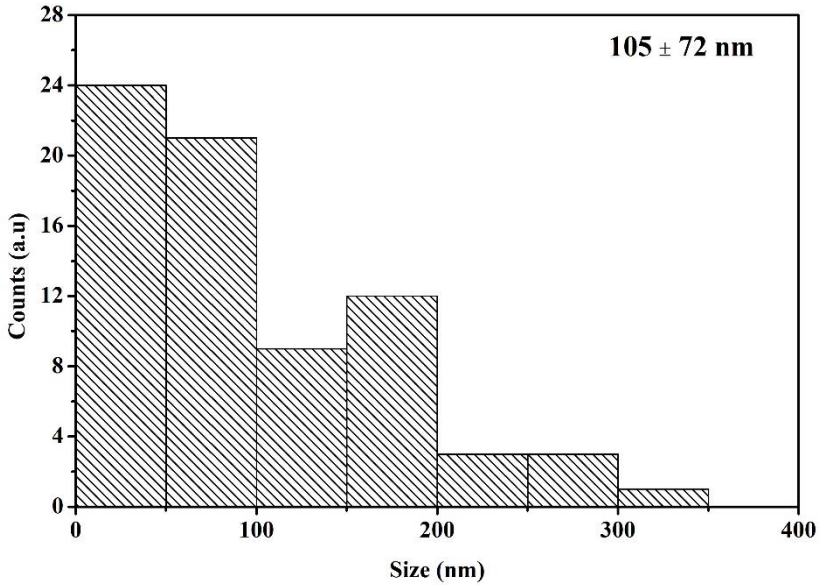

Figure S10. Diameter size distribution of MIL-91(Ti)/GO5wt% post-synthesis.

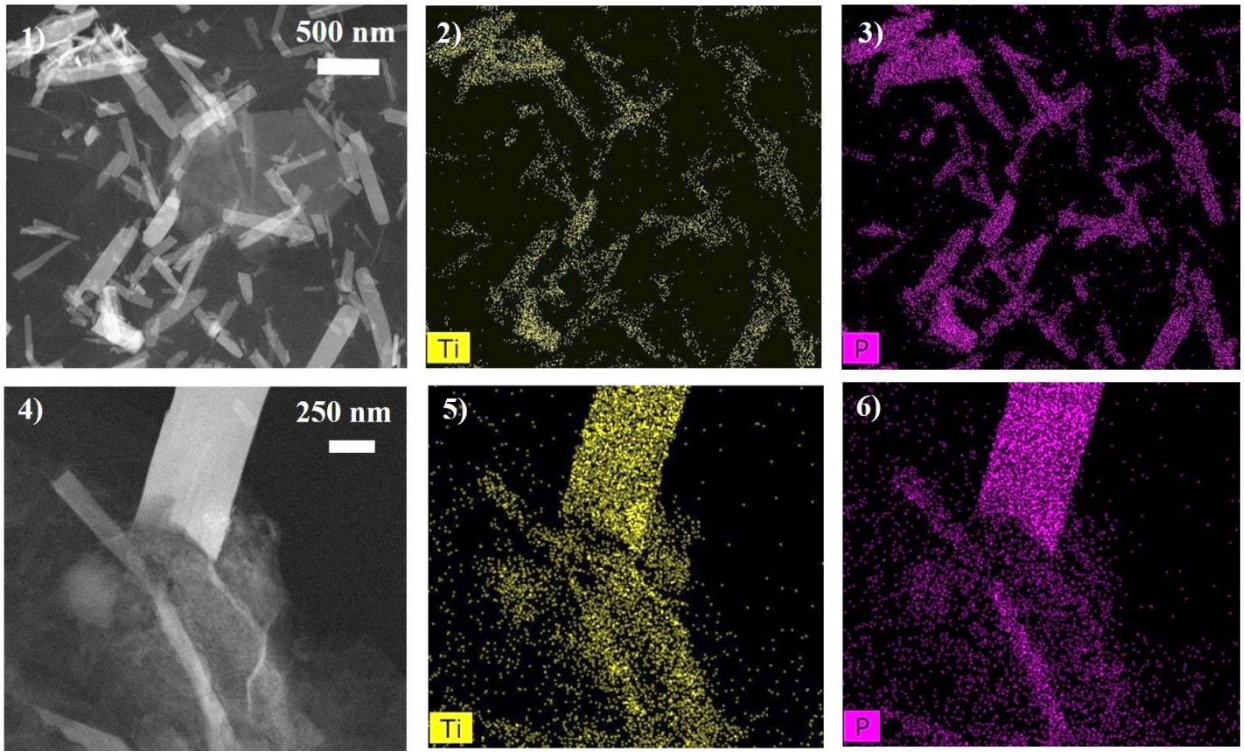

Figure S11. 1) STEM-HAADF image and EDS mapping of 2) titanium (yellow) and 3) phosphorus (pink) of MIL-91(Ti)/GO5wt% post-synthesis. 4) STEM-HAADF image and EDS mapping of 5) titanium (yellow) and 6) phosphorus (pink) of MIL-91(Ti)/GO5wt% *in situ*.

To shed light on the microstructure of the two composites with 5wt% GO, the local environment of Ti atoms was investigated by XPS spectroscopy. Note that the XPS spectra of Ti2p exhibit two peaks because of the LS coupling ($2p_{1/2}$ and $2p_{3/2}$). As shown in Figure S12, only one contribution (represented in pink), was necessary to fit the titanium spectra of the pure MOF as well as the post-synthesis composite (Figure S13.1), in agreement with only one chemical environment, i.e. titanium within the MOF structure. However, when the same fitting parameters were applied to the *in situ* sample, a second contribution was required to fit the experimental spectrum (Figure S13.2). This is in agreement with the EDS results which showed the presence of titanium atoms both from the MOF framework and the metal species grafted on the GO surface.

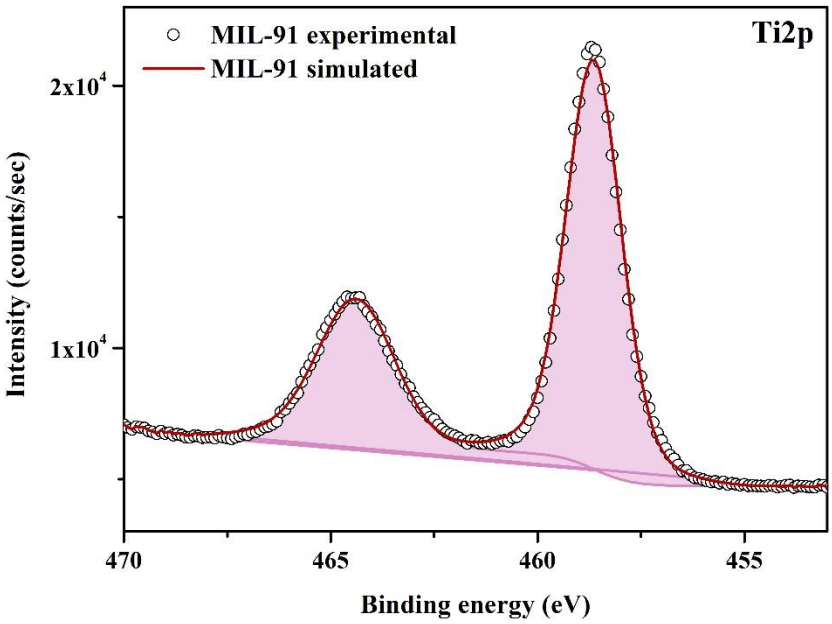

Figure S12. Deconvoluted XPS spectra of Ti2p of pure MIL-91(Ti). The simulated contribution is plotted in pink.

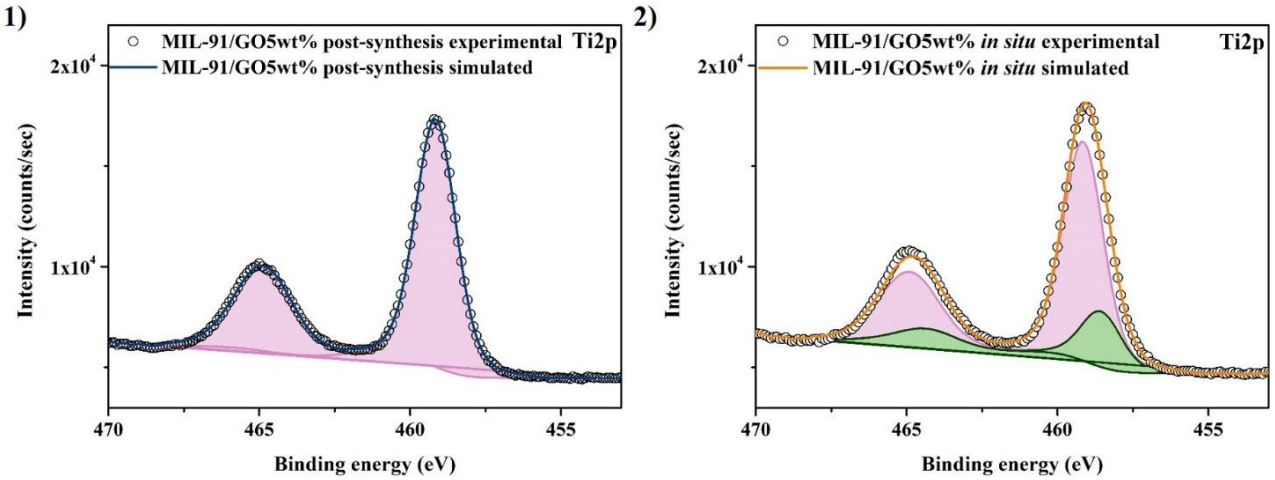

Figure S13. Deconvoluted XPS spectra of Ti2p of 1) MIL-91(Ti)/GO5wt% post-synthesis and 2) MIL-91(Ti)/GO5wt% *in situ*. The simulated contributions are plotted in pink and green.

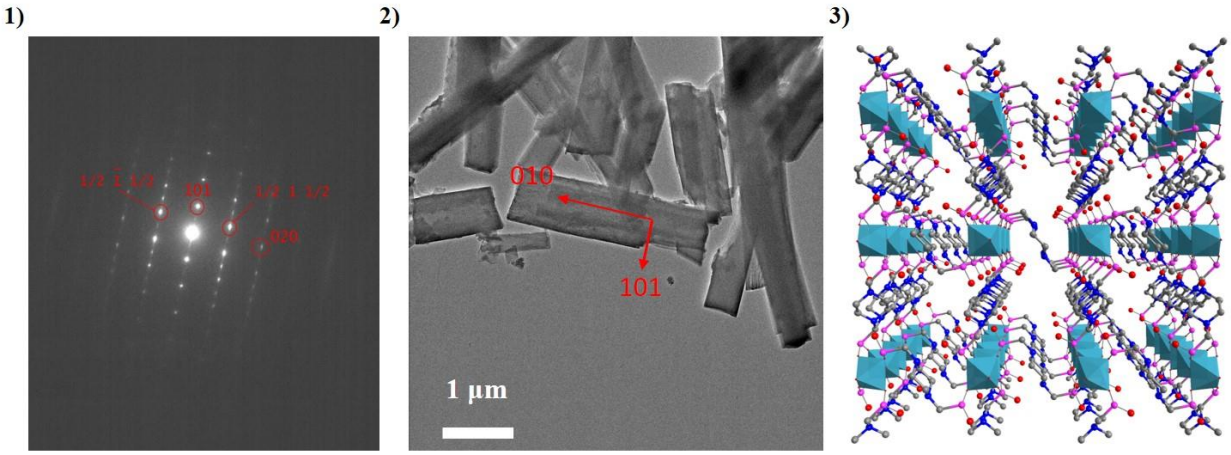

Figure S14. 1) SAED and 2) TEM image of MIL-91(Ti)/GO5wt% *in situ* 3) view along [010] axis of MIL-91(Ti). The Ti octahedron are represented in blue, phosphorus atoms in pink, nitrogen in dark blue, oxygen in red and carbon in grey.

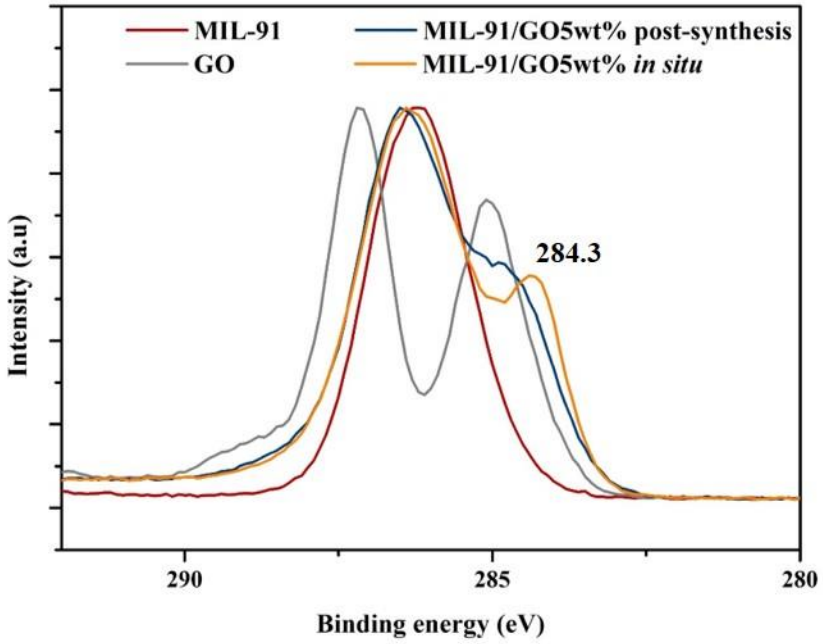

Figure S15. XPS spectra of C1s of pure MIL-91(Ti), pure GO, MIL-91(Ti)/GO5wt% *in situ* and post-synthesis

The XPS C1s spectrum of pure GO is made of several contributions which are summarized in Table S4.

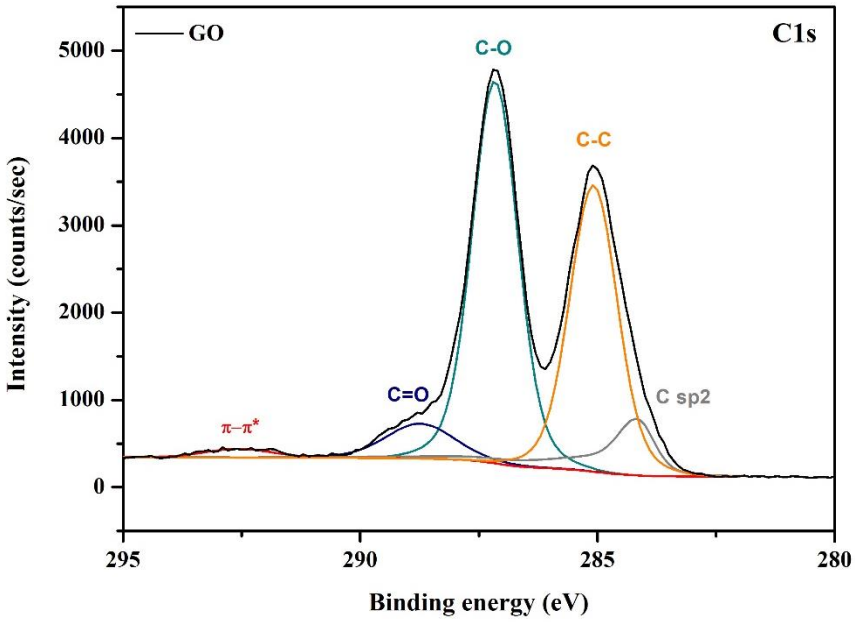

Figure S16. Deconvoluted XPS spectrum of C1s of pure GO.

Table S4. Binding energy of each contribution of the C1s XPS spectrum of pure GO

	Binding energy (eV)
C sp^2	284.3
C-C	285.1
C-O	287.2
C=O	288.8

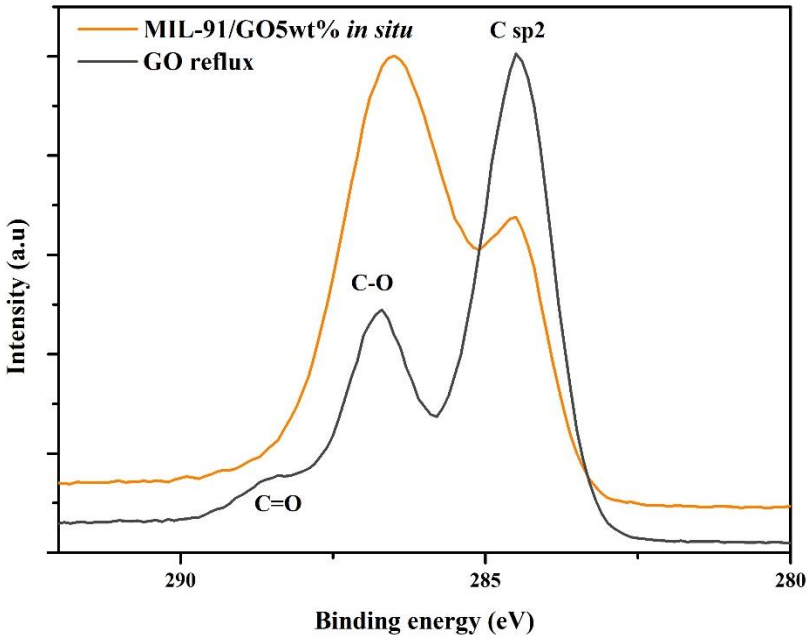

Figure S17. XPS spectra of C1s of MIL-91(Ti)/GO5wt% *in situ* and GO after overnight reflux in water.

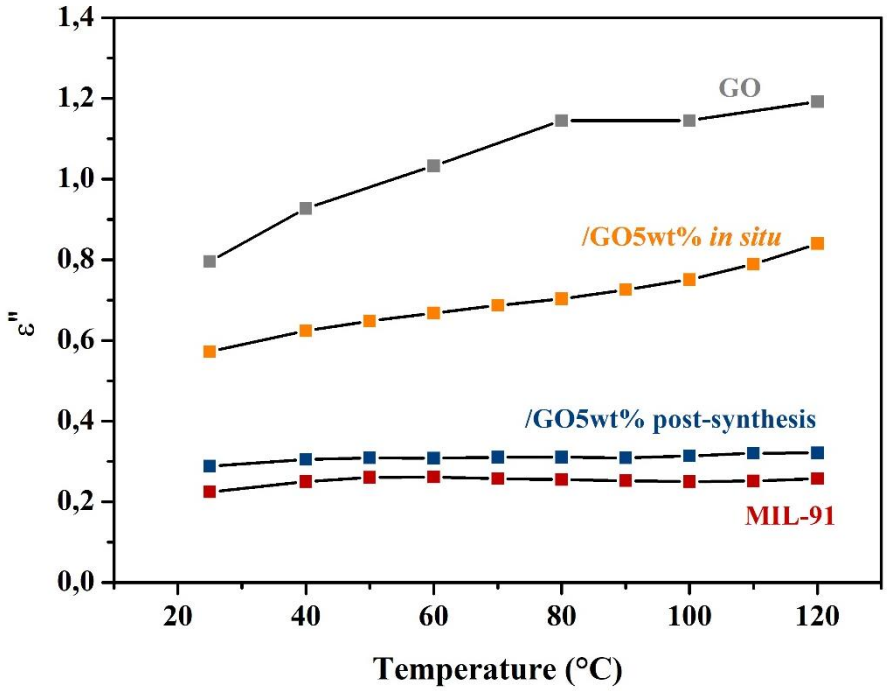

Figure S18. Imaginary part of the permittivity as a function of the temperature of MIL-91(Ti), GO and MIL-91(Ti)/GO5wt% post-synthesis and *in situ*.

Desorption experiments

Pure CO_2 isotherms

The pure CO_2 isotherms between 0 and 1 bar at 303 K of MIL-91(Ti), MIL-91(Ti)/GO5wt% *in situ* composite powder and spheres are shown in Figure S19. All these materials exhibit an isotherm that deviates at very low pressure from a type I Langmuir isotherm, most likely due to a slight internal flexibility of the framework, although to a much lower extent compared to what was observed previously for MIL-91(Al)[5]. The CO_2 adsorption capacity at 0.15 bar is reported in Table S5. The higher adsorption capacity of the *in situ* composite compared to that of the pure MOF (both powders) was attributed to the microporosity created at the MOF/GO interface, in agreement with the N_2 porosimetry at 77 K results.

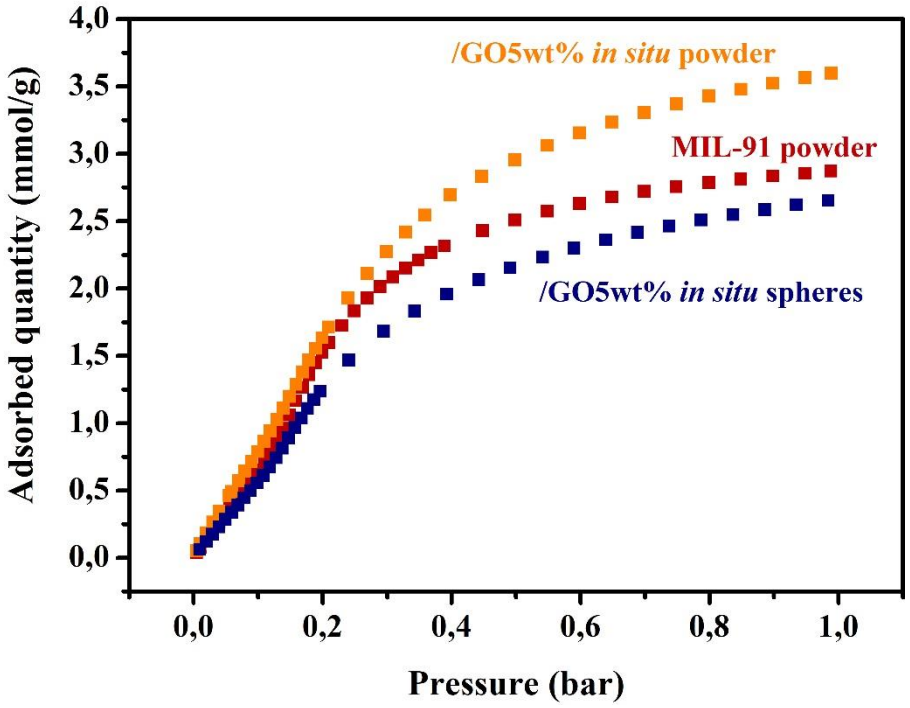

Figure S19. CO_2 isotherms at 303 K of MIL-91(Ti) powder, MIL-91(Ti)/GO5wt% powder and spheres.

Table S5. CO_2 adsorption capacity at 0.15 bar and 303 K of MIL-91(Ti) powder, MIL-91(Ti)/GO5wt% powder and spheres.

	CO_2 adsorption capacity at 0.15 bar, 303 K (mmol/g)
MIL-91(Ti)	1.08
MIL-91(Ti)/GO5wt% *in situ* powder	1.20
MIL-91(Ti)/GO5wt% *in situ* spheres	0.90

During the desorption experiments, the temperature was monitored by an IR camera under MW radiation and with a Pt100 contact temperature probe under conventional heating. Please note that for both MW and convection heating, the given temperatures are those of the column, which explains the observed faster heating under convection compared to MW. Indeed, in the oven, the column is first heated and the heat is then transferred to the MOF/GO composites. On the other hand, the opposite happens with MW; the material is first heated and the heat is then transferred to the column.

As shown in Figure S20, the temperature exceeds 50 °C (but remains under 57 °C) under MW radiation for approximately 100 seconds, before stabilizing around 50 °C. Although this slight overheating might affect the desorption time, it is not the reason behind the faster desorption under MW compared to conventional heating at 50 °C. Indeed, desorption measurements under conventional heating at 80 °C were also performed (Figure S21) and showed that MW desorption at ≈ 50 ° is faster. Therefore, it highlights that CO_2 release is faster under MW radiation compared to convection desorption even at lower temperatures.

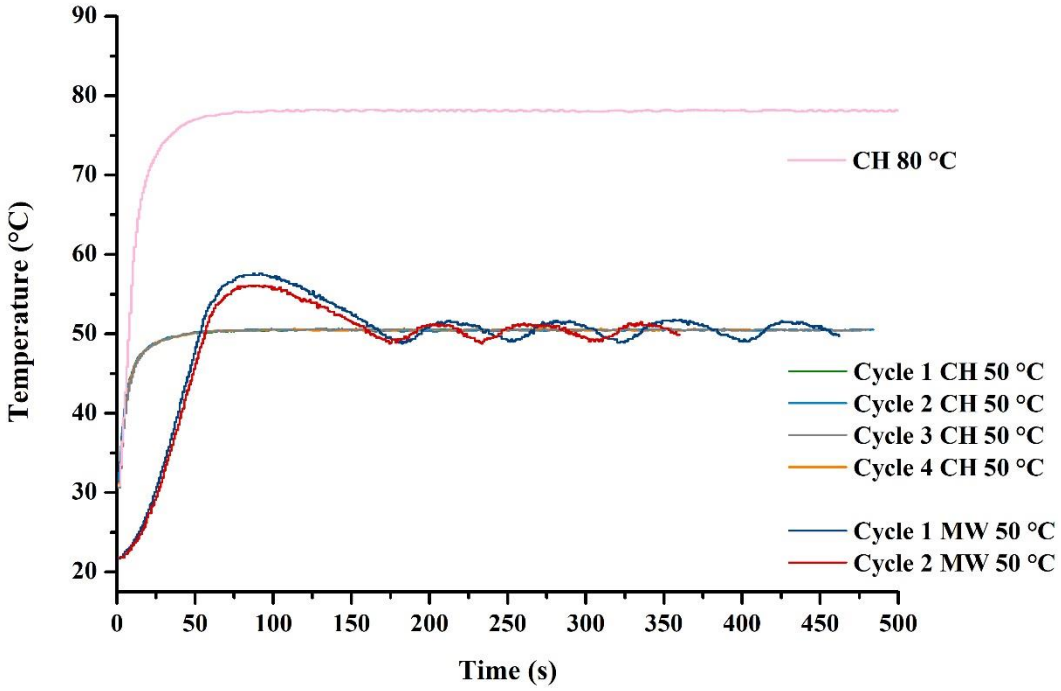

Figure S20. Temperature monitoring under MW radiation and conventional heating (CH) at 50 °C and 80 °C on MIL-91/GO5wt% *in situ* composite.

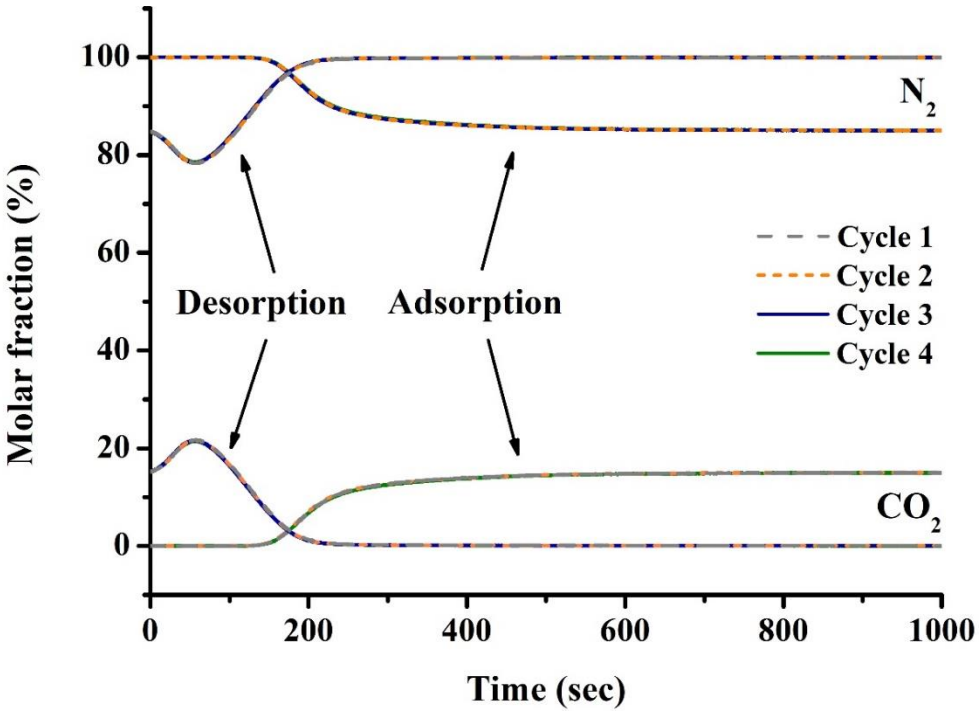

Figure S21. Breakthrough adsorption curves (mixture CO_2/N_2 15/85 molar, atmospheric pressure, 30 °C) and desorption curves under conventional heating (CH) at 80 °C over 4 cycles on MIL-91/GO5% *in situ* composite.

We determined the CO_2 adsorption and desorption amounts by integrating the adsorption and desorption breakthrough curves as follows:

$$q_{CO2,ads} = \frac{Q_{tot}}{m}\int_0^t \left(y_{CO2,in} - y_{CO2}(t)\right) dt$$

$$q_{CO2,des} = \frac{Q_{tot}}{m}\int_0^t y_{CO2}(t) dt$$

With $q_{CO2,ads}$, the CO_2 adsorbed amounts (mmol/g), $q_{CO2,des}$, the CO_2 desorbed amounts (mmol/g), Q_{tot}, the total molar flowrate (mol/s), $y_{CO2,in}$, the initial CO_2 concentration at the inlet (15%), $y_{CO2}(t)$, the CO_2 concentration at time, *t*, and *m*, the mass of adsorbent (g).

All values obtained are equivalent (the difference can be explained by the experimental uncertainties) (Table S6), which confirms that the adsorption capacity is maintained as already shown by the reproducibility of the adsorption/desorption cycles.

Table S6. CO_2 adsorbed and desorbed amounts for MIL-91(Ti)/GO5wt%

	CO_2 adsorbed and desorbed amounts (mmol/g) during heating at 50 °C	CO_2 adsorbed and desorbed amounts (mmol/g) during heating at 80 °C	CO_2 adsorbed and desorbed amounts (mmol/g) during MW heating
Cycle 1	0.89/0.89	0.86/0.87	0.87/0.85
Cycle 2	0.86/0.87	0.88/0.86	0.89/0.88
Cycle 3	0.89/0.88	0.87/0.88	/
Cycle 4	0.89/0.89	0.89/0.89	/

UiO-66-btc(Zr)/GO

The successful formation of the MOFs within the *in situ* composites was confirmed by PXRD (Figure S22).

The N_2 adsorption porosimetry at 77 K of the different UiO-66-btc(Zr)/GO *in situ* composites with 5 and 10wt% GO show an increase of BET surface area compared to the pure MOF (Figure S23). It suggests that, similarly to what was observed with MIL-91(Ti)/GO composites, extra porosity is created at the interface, leading to higher BET surface areas despite the presence of non-porous GO. With 20wt% GO, a BET surface area of 660 m^2/g was obtained, higher than the theoretical value taking into account 20wt% of non-porous material (590 m^2/g). Therefore, with 20wt% GO, the extra porosity is probably not sufficient enough to entirely balanced the presence of GO.

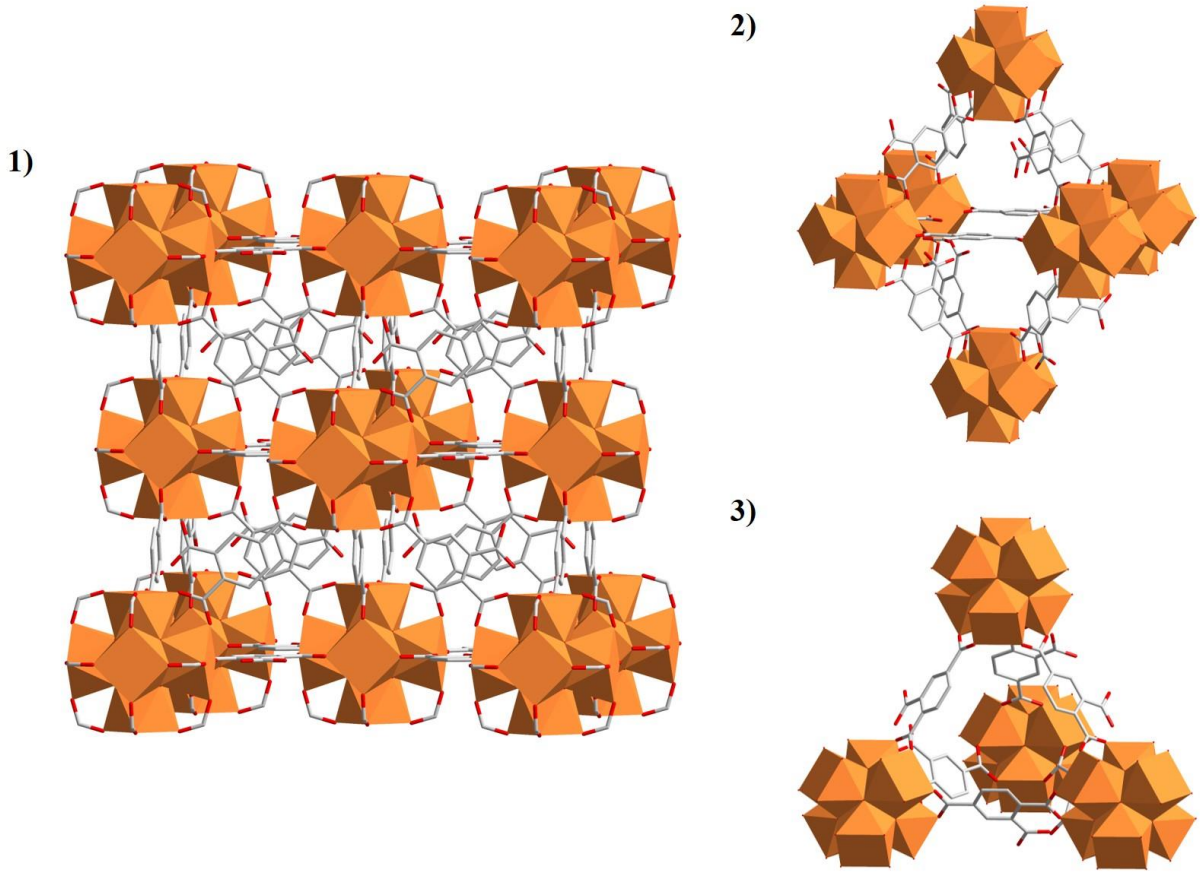

Figure S22. 1) Crystal structure of UiO-66-btc(Zr) with the representation of 2) an octahedral cavity and 3) a tetrahedral cavity. The Zr clusters are represented in orange, carbon atoms in grey and oxygen atoms in red.

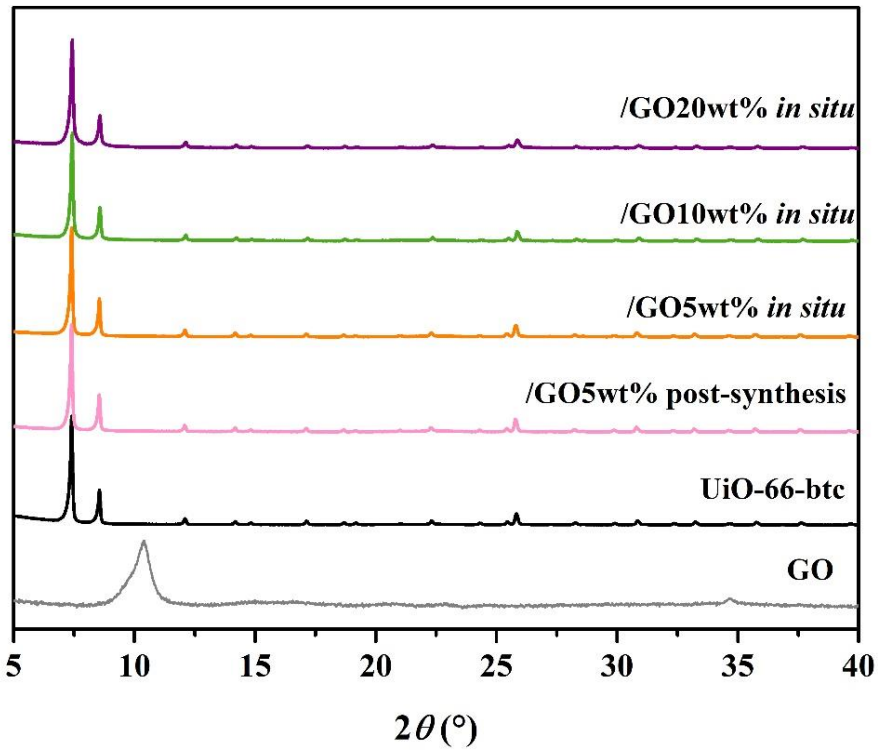

Figure S23. PXRD patterns of GO, UiO-66-btc(Zr), UiO-66-btc(Zr)/GO5wt% post-synthesis and UiO-66-btc(Zr)/GO5, 10 and 20wt% *in situ*.

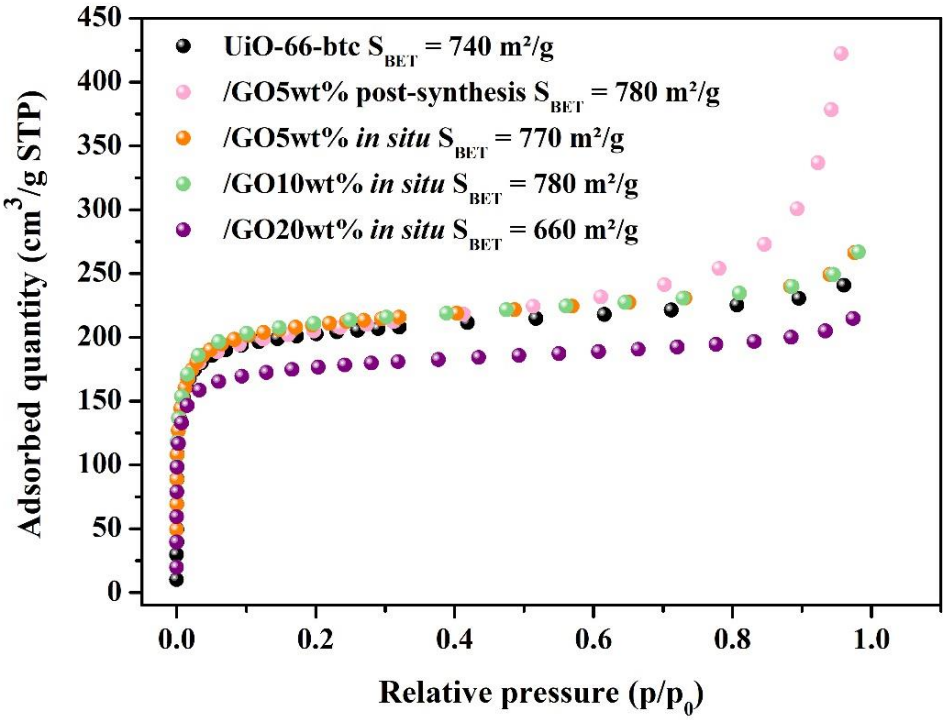

Figure S24. Nitrogen adsorption isotherms at 77 K of UiO-66-btc(Zr) and UiO-66-btc(Zr)/GO composites.

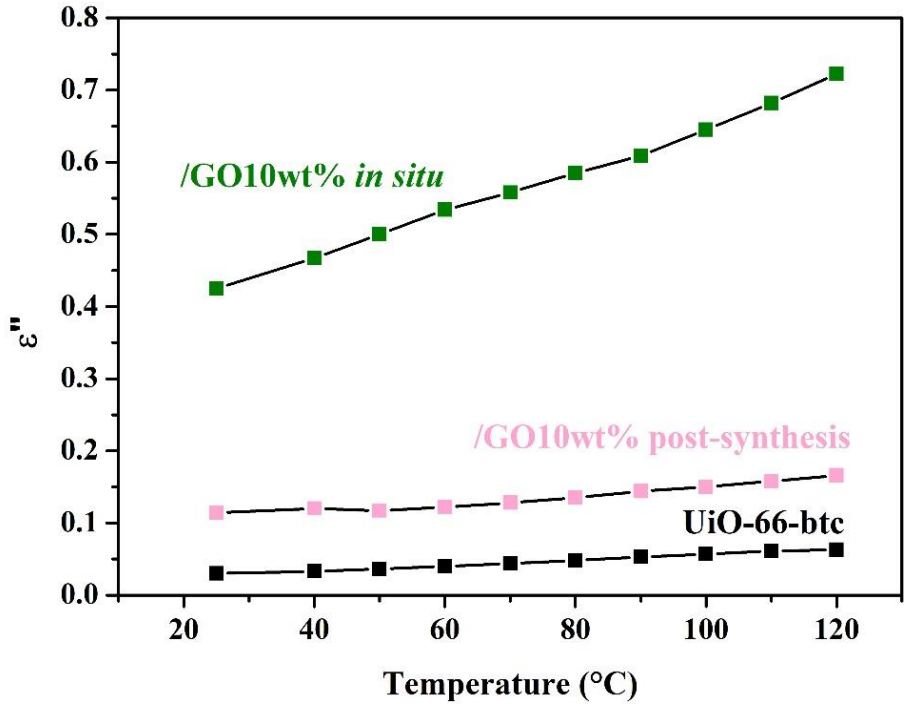

Figure S25. imaginary part of the permittivity as a function of the temperature of UiO-66-btc(Zr), UiO-66-btc(Zr)/GO10wt% post-synthesis and *in situ.*

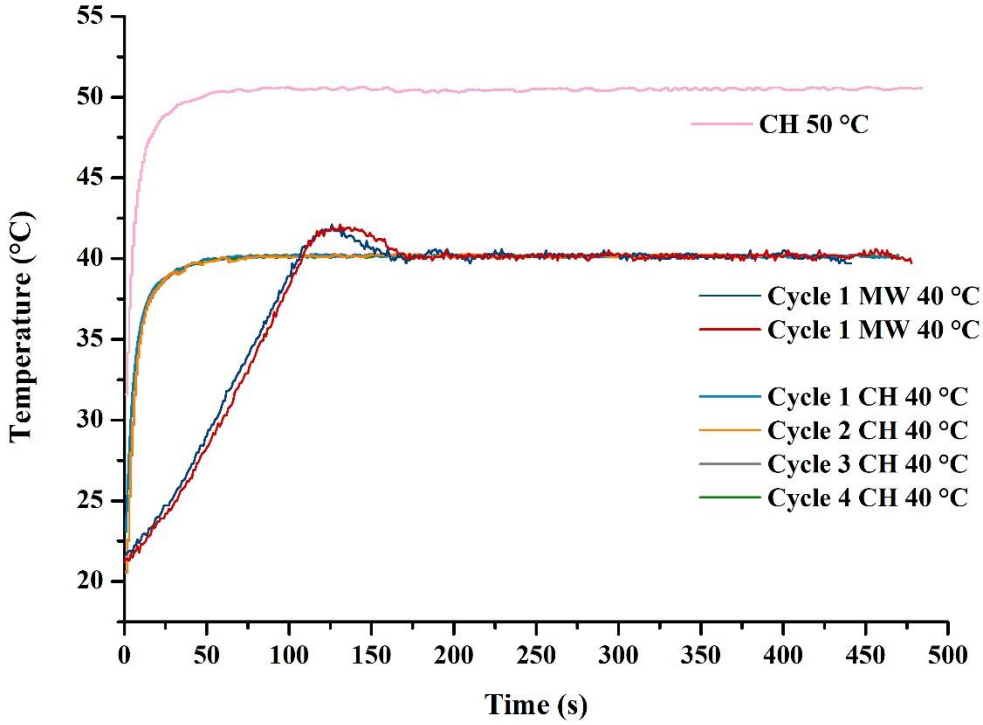

Figure S26. Temperature monitoring under MW radiation and conventional heating (CH) at 40 °C and 50 °C on UiO-66-btc(Zr)/GO10wt% *in situ* composite.

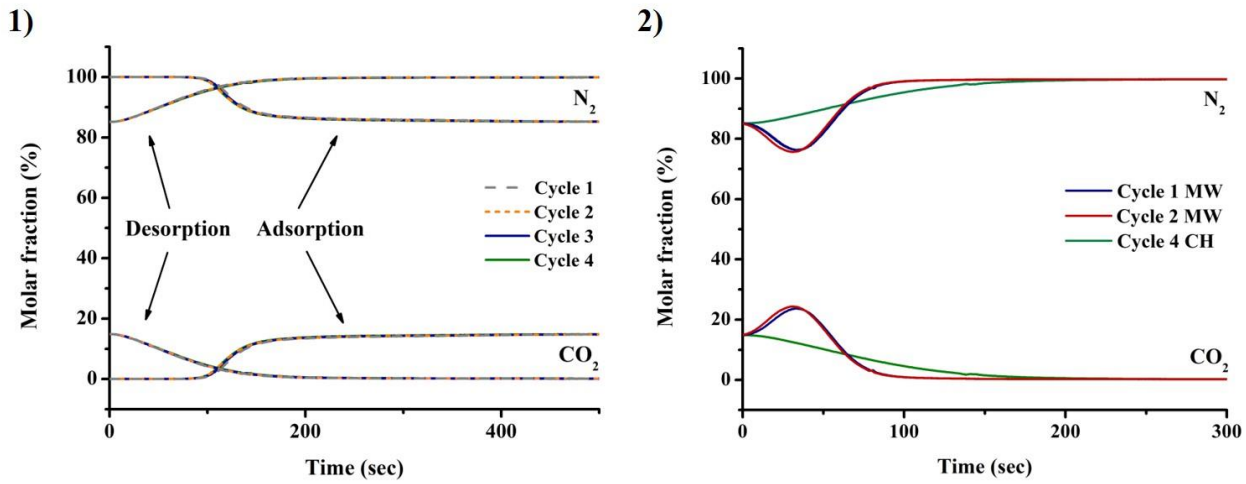

Figure S27. 1) Breakthrough adsorption curves (mixture CO_2/N_2 15/85 molar, atmospheric pressure, 30 °C) and desorption curves under conventional heating (CH) at 50 °C over 4 cycles and 2) Breakthrough desorption curves under MW radiation at 40 °C over 2 cycles compared with the fourth breakthrough desorption curve obtained under CH at 50 °C on UiO-66(Zr)-btc/GO10wt% *in situ* composite.

The adsorbed and desorbed CO_2 amounts were obtained by using the same method as for MIL-91(Ti)/GO composite. The values are similar (Table S7), confirming the good reproducibility of the cycles under MW and conventional heating.

Table S7. CO_2 adsorbed and desorbed amounts for UiO-66-btc(Zr)/GO10wt%

	CO_2 adsorbed and desorbed amounts (mmol/g) during heating at 40°C	CO_2 adsorbed and desorbed amounts (mmol/g) during heating at 50°C	CO_2 adsorbed and desorbed amounts (mmol/g) during MW heating
Cycle 1	0.35/0.33	0.36/0.35	0.35/0.32
Cycle 2	0.34/0.35	0.34/0.36	0.36/0.38
Cycle 3	0.37/0.34	0.35/0.33	0.37/0.34
Cycle 4	0.35/0.33	0.36/0.34	0.36/0.37

References

1. Kumar, R.; Jayaramulu, K.; Maji, T. K.; Rao, C. N. R., Hybrid nanocomposites of ZIF-8 with graphene oxide exhibiting tunable morphology, significant CO2 uptake and other novel properties. *Chemical Communications* **2013,** *49* (43), 4947-4949.
2. Liu, N.; Huang, W.; Zhang, X.; Tang, L.; Wang, L.; Wang, Y.; Wu, M., Ultrathin graphene oxide encapsulated in uniform MIL-88A(Fe) for enhanced visible light-driven photodegradation of RhB. *Applied Catalysis B: Environmental* **2018,** *221*, 119-128.
3. Amirov, R. R.; Shayimova, J.; Nasirova, Z.; Dimiev, A. M., Chemistry of graphene oxide. Reactions with transition metal cations. *Carbon* **2017,** *116*, 356-365.
4. Chen, B.; Zhu, Y.; Xia, Y., Controlled in situ synthesis of graphene oxide/zeolitic imidazolate framework composites with enhanced CO2 uptake capacity. *RSC Advances* **2015,** *5* (39), 30464-30471.
5. Llewellyn, P. L.; Garcia-Rates, M.; Gaberová, L.; Miller, S. R.; Devic, T.; Lavalley, J.-C.; Bourrelly, S.; Bloch, E.; Filinchuk, Y.; Wright, P. A.; Serre, C.; Vimont, A.; Maurin, G., Structural Origin of Unusual CO2 Adsorption Behavior of a Small-Pore Aluminum Bisphosphonate MOF. *The Journal of Physical Chemistry C* **2015,** *119* (8), 4208-4216.